A density functional study of the pressure induced phase transition in $LiYF_4$

2006 J. Phys.: Condens. Matter 18 2429

(http://iopscience.iop.org/0953-8984/18/8/009)

INSTITUTE OF PHYSICS PUBLISHING JOURNAL OF PHYSICS: CONDENSED MATTER

J. Phys.: Condens. Matter **18** (2006) 2429–2441 doi:10.1088/0953-8984/18/8/009

A density functional study of the pressure induced phase transition in $LiYF_4$

B Minisini, L El Hadj, M Lontsi Fomena, N Van Garderen and F Tsobnang

Institut Supérieur des Matériaux et Mécaniques Avancés du Mans, 44 Avenue Bartholdi, 72000 Le Mans, France

E-mail: bminisini@ismans.univ-lemans.fr

Received 23 May 2005, in final form 16 January 2006
Published 10 February 2006
Online at stacks.iop.org/JPhysCM/18/2429

Abstract

An investigation of the pressure induced phase transition from the scheelite phase ($I4_1/a, Z = 4$) to the fergusonite-like phase ($I2/a, Z = 4$) and to the $LaTaO_4$ phase ($P2_1/c, Z = 4$) of $LiYF_4$ is presented. Employing density functional theory (DFT) within the generalized gradient approximation, the structures were relaxed for a pressure range of 0–20 GPa without imposed symmetry. The influence of pressure on the lattice vibrational spectrum of the scheelite phase ($I4_1/a, Z = 4$) was evaluated using the direct approach, i.e. using force constants calculated from atomic displacements. This work tends to confirm the transformations $I4_1/a \rightarrow C2/c \rightarrow P2_1/c$. At 20 GPa, a $P2_1/c$ structure with a pentacoordinated lithium cation is found to be the most stable phase. This structure is compatible with a transition driven by a B_g zone-centre soft optic mode linked to a soft acoustic mode along the $[11\bar{1}]$ direction as observed from the evolution of the phonon dispersion curves as a function of pressure.

1. Introduction

Due to its importance as a host material for laser applications, undoped and doped $LiYF_4$ has received considerable attention over the past decade [1–3]. It is now commonly accepted that the scheelite phase ($I4_1/a, Z = 4$) is stable over the 30–1000 K range [4]. The symmetry elements of this space group are a fourfold screw axis and a glide plane normal to it. Most of the recent studies were performed at ambient pressure conditions, so the transition pressures as well as the high-pressure phases are in need of further investigation. Blanchfield *et al* [6] did hydrostatic pressure studies from 0 to 0.16 GPa on second-order elastic constants and thereby showed first acoustic mode softening. However, no phase transition information was provided. More recently, Sarantopoulou *et al* [4] noticed a discontinuity in the Raman active modes as a function of the pressure at 7 GPa. Changes in Li–F bond distances rather than Y^{3+}–LiF_4^{3-}

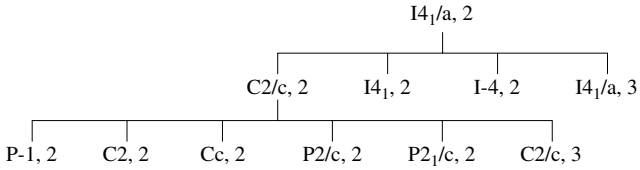

Figure 1. Tree of subgroup/group relationship for $I4_1/a$ structure. The numbers in italic indicate the index of transformation [5].

were assumed to be the cause of this anomaly, the structure remaining tetragonal. No other changes were observed up to a pressure of 16 GPa. From x-ray powder diffraction measurement of $LiYF_4$ and of $CaWO_4$, Errandonea *et al* [7] proposed the existence of a reversible phase transition of two scheelite polytypes induced by LiF_4 polyhedral tilting at 6 GPa. Moreover, Grzechnik *et al* [8] identified two pressure induced phase transitions. The first transition at 10 GPa was supposed to lead to the fergusonite ($I2/a$, $Z = 4$) structure. The second transition was detected around 17 GPa. It was impossible for the authors to determine reliable data for cell parameters, but they proposed a list of possible crystallographic structures.

Based on these experimental data, some theoretical studies were subsequently undertaken. Sen *et al* [9, 10] observed two-phase transitions using an empirical rigid ion model (RIM). The first transition near 5 GPa was a second order phase transition without a volume decrease. Moreover, the crystallographic structure was observed to depend on temperature. Below 400 K the LaTaO ($P2_1/c$, $Z = 4$) structure was found to be the most stable; however, the fergusonite ($I2/a$, $Z = 4$) structure was the most stable at higher temperature. The second transition near 16 GPa was found to be a first order phase transition with a 6% volume decrease, leading to a LaTaO ($P2_1/c$, $Z = 4$) structure. However, employing density functional theory (DFT), Li *et al* [11] found a transition at 0 K and 9.3 GPa leading to fergusonite ($I2/a$, $Z = 4$) structure and a second one at 17.6 GPa leading to wolframite ($P2/c$, $Z = 2$) structure. As presented in figure 1, all these structures belong to the tree of subgroup/group relationships obtained from the Bilbao Crystallographic Server [5].

In this work we present a DFT analysis of structural properties of $LiYF_4$ scheelite ($I4_1/a$, $Z = 4$), fergusonite ($I2/a$, $Z = 4$), wolframite ($P2/c$, $Z = 2$) and $LaTaO_4$ ($P2_1/c$, $Z = 4$) structures (figure 2) under pressure at 0 K. The structures were optimized under pressure ranging from 0 to 20 GPa without imposing any symmetry restrictions. Structural parameters and x-ray powder diffraction patterns of the optimized cells were analysed. Enthalpies were calculated to evaluate the most stable phase under pressure. In addition, vibrational properties and elastic constants of the optimized structures from the initial scheelite ($I4_1/a$, $Z = 4$) structure were calculated under pressure up to 20 GPa.

2. Simulation

All calculations were carried out using density functional theory (DFT) [12, 13] as implemented in the Vienna *ab initio* simulation package (VASP) [14], part of the MedeA modelling interface[1]. The exchange–correlation functional was approximated by the gradient corrected form proposed by Perdew and Wang [15]. The electronic degrees of freedom were described using the projector augmented wave method (PAW) [16, 17]. Electronic convergence was set up at 10^{-6} eV. Sampling of the Brillouin zone was performed with the Monkhorst–Pack scheme [18].

[1] Materials Design Angel Fire NM.

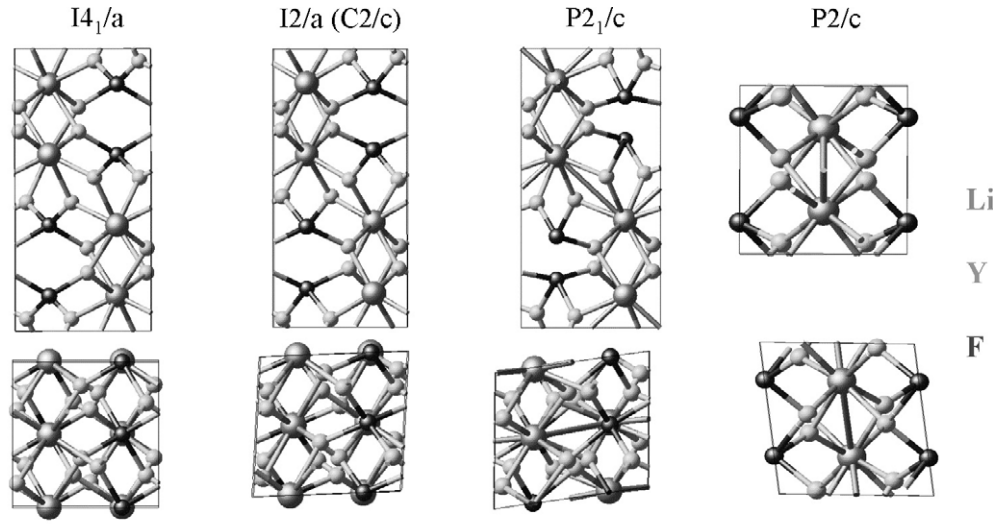

a=c (Å)	5.16
b (Å)	10.74
α=γ =β(°)	90

a (Å)	5.16
b (Å)	10.41
c (Å)	4.78
α=γ (°)	90
β (°)	95.27

a (Å)	5.22
b (Å)	10.43
c (Å)	4.57
α=γ (°)	90
β (°)	98.6

a (Å)	4.98
b (Å)	5.43
c (Å)	5.30
α=γ (°)	90
β (°)	94.96

Figure 2. Crystal structures of $LiYF_4$.

2.1. Structure optimization

Experimental structural parameters for scheelite ($I4_1/a, Z = 4$) [19] and fergusonite ($I2/a, Z = 4$) [8], were used to build our models. The $P2_1/c$ ($Z = 4$) was built from results obtained by Sen *et al* [10] using classical molecular dynamics. The $1 \times 2 \times 1$ supercell of wolframite ($P2/c, Z = 2$) was constructed based on calculated data by Li *et al* [11]. In the literature cited above, the labelling for the tetragonal cell axis is different between the structures. For clarity and to follow the convention in the literature [8, 10] we have renamed the unit cell axes a, b and c of the $I4_1/a$ structures as c, a and b respectively. Moreover, to define the fergusonite ($I2/a, Z = 4$) structure we will use the revised space group $C2/c$, $Z = 4$.

Full structural relaxations of the four initial structures defined earlier were performed at 0, 2, 4, 6, 10, 12, 14, 16, 18 and 20 GPa, except for scheelite, where calculations were performed until −6 GPa, and for the wolframite supercell, where a single calculation was performed at 20 GPa. The symmetries of all the structures were reduced to P1. So all atoms were considered to be symmetrically inequivalent in order to allow for structural phase transition. Calculations were considered converged when residual forces were less than 2 meV $Å^{-1}$. At 0 GPa, the residual bulk stresses were smaller than 25 MPa for all structures. Volume relaxation is not an easy task due to the basis set incompleteness [20]. This is why we choose a high precision calculation with an energy cut-off of 700 eV, which is 40% higher than used in the previous study [11]. The total energy changes by less than 3 meV/$LiYF_4$ on increasing the cut-off from 700 to 750 eV. Moreover, a convergence test concluded that a k-spacing of 0.5 $Å^{-1}$ was sufficient to obtain a total energy convergence within 0.1 meV/cell compared to 0.2 $Å^{-1}$ at 0 GPa. To get unambiguous energies, single point energy calculations with the same parameters

as described above were performed on all the optimized structures. The energy are given in kJ mol^{-1} for $LiYF_4$.

To name the optimized structures we define a nomenclature as follows: S_P^{sym}. The superscript sym stands for the symmetry of the structure before optimization; the P subscript stands for the pressure imposed during the optimization.

2.2. Lattice dynamic calculation

The lattice vibrational properties were calculated within the harmonic approximation, using the PHONON code [21]. Using PHONON the force constant matrix was calculated via atomic displacements with an interaction range of 7 Å. The asymmetric atoms were displaced by ± 0.03 Å leading to 14 new structures. The dynamical matrix was obtained from the forces calculated via the Hellmann–Feynman theorem. The selected k-point spacing led to six symmetry independent k-points and a high precision calculation with a plane-wave cut-off of 550 eV was used to describe the electronic valence states. The longitudinal optical (LO) and transversal optical (TO) mode splitting was not investigated in this work. Consequently, only TO modes at the $\mathbf{\Gamma}$ point were obtained.

2.3. Mechanical property calculation

The volume versus pressure curve has been fitted with the Birch–Murnaghan equation of state for $S_{-6<P<14}^{I4_1/a}$ to evaluate the equilibrium volume and the bulk modulus. Moreover, the elastic constants have been calculated for $S_P^{I4_1/a}$ from the stress evaluated on six strained cells [22]. The applied strains were $e_{xx} = \pm 0.01$, $e_{zz} = \pm 0.01$, $e_{xy} = 0.01$ and $e_{yz} = 0.01$ with the other strain components zero respectively for the six strained cells. The calculation parameters were the same as in section 2.1. For a crystal belonging to the TII Laue group, the elastic stiffness constant matrix referred to the crystallographic axis (X, Y, Z) reference frame is

$$C_{ij} = \begin{pmatrix} c_{11} & c_{12} & c_{13} & 0 & 0 & c_{16} \\ c_{12} & c_{22} & c_{13} & 0 & 0 & -c_{16} \\ c_{13} & c_{13} & c_{33} & 0 & 0 & 0 \\ 0 & 0 & 0 & c_{44} & 0 & 0 \\ 0 & 0 & 0 & 0 & c_{44} & 0 \\ c_{16} & -c_{16} & 0 & 0 & 0 & c_{66} \end{pmatrix}.$$

The sign of the elastic coefficient C_{16} depends on the choice of the $+Z$ axis or $+Y$ axis respectively before and after relabelling. To evaluate the sense of the axis we used the standard convention employed for the scheelite structures [23]. Complete discussion of this topic is available elsewhere [24].

3. Results

3.1. Structural properties

The pressure dependence of the lattice parameters is presented in figure 3. From these results it is worth noting that during the lattice optimization the three different initial structures converged to one and the same set of cell parameters for pressures below 10 GPa (figure 3(a)). The equilibrium cell parameters at 0 GPa are $a = c = 5.23$ Å, $b = 10.83$ Å and $\alpha = \beta = \gamma = 90°$, giving a cell volume of 296 Å^3. This volume is 3.7% higher than the experimental one, confirming the overcorrection of the GGA on local density approximation as discussed by Li *et al* [11] for this structure. From fitting the Birch–Murnaghan equation of state, the

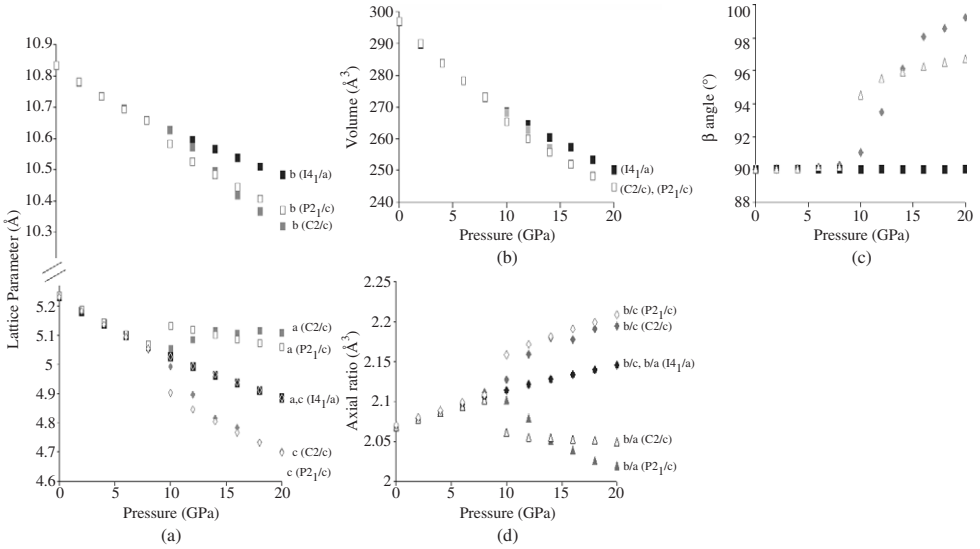

Figure 3. Lattice parameters versus pressure for the $I4_1/a$ ($Z = 4$), $C2/c$ ($Z = 4$) and $P2_1/c$ ($Z = 4$) initial structures.

experimental volume of 286 Å^3 is obtained here for an applied pressure of 3.15 GPa. The difference in volume of the three optimized structures below 8 GPa does not exceed 0.1% (figure 3(b)). Between 10 and 14 GPa, the three volumes are distinct. But from 16 GPa, the volumes of $S^{C2/c}_{P=16}$ and $S^{P2_1/c}_{P=16}$ become similar and are respectively 1.78% and 1.96% lower than the $S^{I4_1/a}_{P=16}$ volume.

Focusing on cell parameters we can notice that the decrease of volume is associated with a distortion of the $S^{C2/c}_{P\geqslant 10}$ and $S^{P2_1/c}_{P\geqslant 10}$ cell. At 10 GPa an important discontinuity is visible for a, b, c and β parameters for $S^{P2_1/c}_{P=10}$. Afterwards, the evolution of a, b and c parameters for $S^{I4_1/a}_{P>10}$ and $S^{P2_1/c}_{P>10}$ is similar. Figure 3(c) shows that the angle β after an abrupt increase up to 94° converges to 97°. The evolution is more progressive for $S^{C2/c}_{P>10}$ around 10 GPa. However, the dependence of the parameters on the pressure is more pronounced at high pressure than for the other structures. This is why, from 16 GPa a, b and β parameters of $S^{C2/c}_{P>16}$ are the highest. The asymmetric behaviour of the inequivalent axes for $S^{C2/c}_{P>10}$ and $S^{P2_1/c}_{P>10}$ is visible in figure 3(d).

These differences in the cell parameters affect the theoretically derived x-ray patterns plotted in figure 4. A wavelength of 0.4203 Å was used, to be consistent with the study of Grzechnik *et al* [8]. Until 10 GPa, the spectra of the optimized structures from initial $S^{I4_1/a}_{P<10}$, $S^{C2/c}_{P<10}$ and $S^{P2_1/c}_{P<10}$ are very similar. So from these different results, it appears that the initial structures relax to the same structure at low pressure.

As a result of the structural parameter changes observed from 10 GPa upwards, the {110} peak at $2\theta = 5.11°$ splits for $S^{P2_1/c}_{P>10}$ and $S^{C2/c}_{P>10}$. The splitting remains over the whole pressure range and, based on the more intense peaks, the similarities of the two patterns are striking. At 20 GPa, the difference between the second peak and the third peak observed for $S^{P2_1/c}_{P=20}$ and $S^{C2/c}_{P=20}$ is 2.29°, in agreement with the measured value [8]. Concerning the wolframite $S^{P2/c}_{P=20}$ at 20 GPa, the difference between the first and the second peak is 1.40° and the general shape of the pattern seems incompatible with the experimental patterns [8]. Moreover, from recent

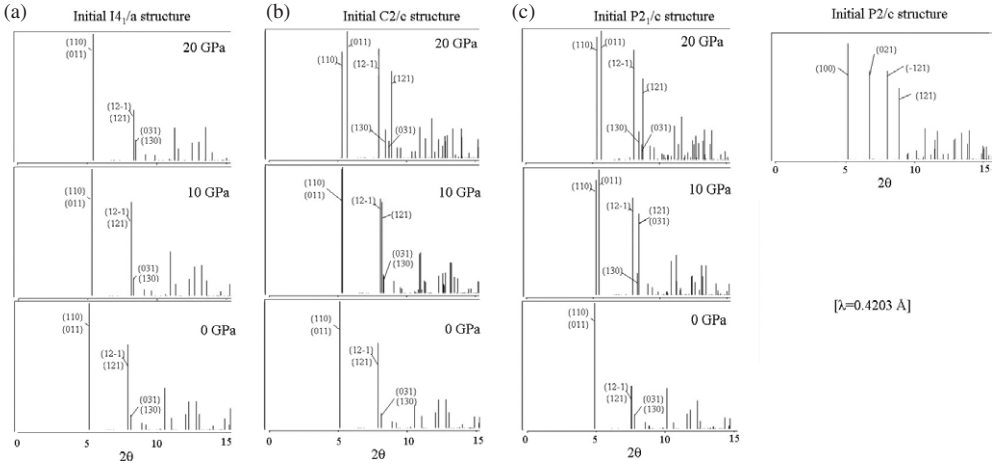

Figure 4. X-ray powder diffraction patterns of P1 optimized structures at different pressures. The initial structures were built from (a) $I4_1/a$, (b) $C2/c$ and (c) $P2_1/c$ space group structures.

studies the transformation from fergusonite to wolframite seems to be excluded for AMX_4 compounds [29], so we excluded this structure from further consideration.

As the relaxed structures at low pressure are the same, we focused on the evolution of the interatomic distances as a function of the pressure for $S_P^{P2_1/c}$ structures, figure 5. At 0 GPa, the Li–F bonds distances in the LiF_4 tetrahedra were 1.92 Å. In the YF_8 octahedra, the four first neighbours are situated at 2.26 Å and the distance to the four second neighbours is 2.32 Å. From 10 GPa, the distances between the lithium and the second neighbours are different, indicating a breaking of the symmetry. At 20 GPa, the Li–F distances lie between 1.79 and 1.84 Å. Further, one of the second neighbours initially situated at 2.93 Å is now at 1.95 Å. Consequently, Li can be assumed as pentacoordinated, the tetrahedra being transformed into a distorted trigonal bipyramidal shape. Concerning Y–F distances, from 10 GPa we can notice an inequivalence of the fluorine atoms since the seven bond lengths are different, notifying a breaking of the symmetry. At 20 GPa, the distances of the eight nearest neighbours are shorter compared to those at low pressure. Following the convention in the literature [7], the cation coordination of $LiYF_4$ is (8-5). This result confirms the hypothesis of the existence of an intermediate structure between (8-4) and (8-6) suggested by Errandonea *et al* [7]. However this structure is different from that calculated by Sen and Chaplot [9], leading to Li and Y octahedrally and tenfold coordinated, respectively, to the fluorine atoms.

As described by Blanchfield *et al* [24], the fluorine framework is rotated by an angle Φ about the b axis. The evolution of the angle Φ as a function of the pressure is presented in figure 6 for all three systems studied. A value of 30.3° is obtained for $S_{P=0}^{C2/c}$ and $S_{P=0}^{P2_1/c}$ at ambient pressure that is in agreement with the experimental value [24]. However, the angle evaluated for $S_{P=0}^{I4_1/a}$ is 3% higher than the other structures. Concerning $S_P^{I4_1/a}$, the evolution of Φ is progressive with an increase of 0.2° per 2 GPa over the pressure range shown in figure 6. For $S_P^{C2/c}$ we notice a discontinuity at 14 and 16 GPa with an increase going up to 0.6°. Concerning $S_P^{P2_1/c}$, the trend is different. Between 0 and 12 GPa, the angle becomes larger with the most important increase at 10 GPa. Then from 14 GPa upwards the angle decreases down to 30.7° at 20 GPa.

Cell parameters and atomic distortions can lead to a change of symmetry. Table 1 gives the symmetry of the fully optimized structures with a tolerance of 0.01 Å. The symmetry of

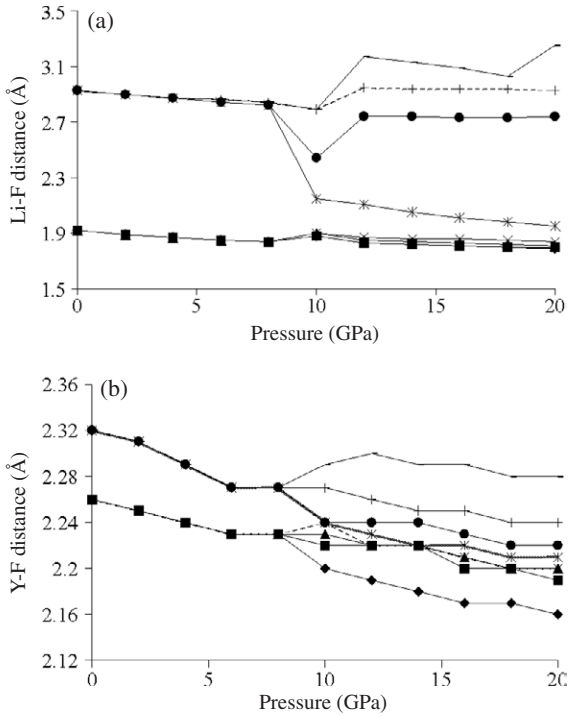

Figure 5. Interatomic distances versus pressure for the $P2_1/c$ ($Z = 4$) initial structures: (a) Li–F; (b) Y–F.

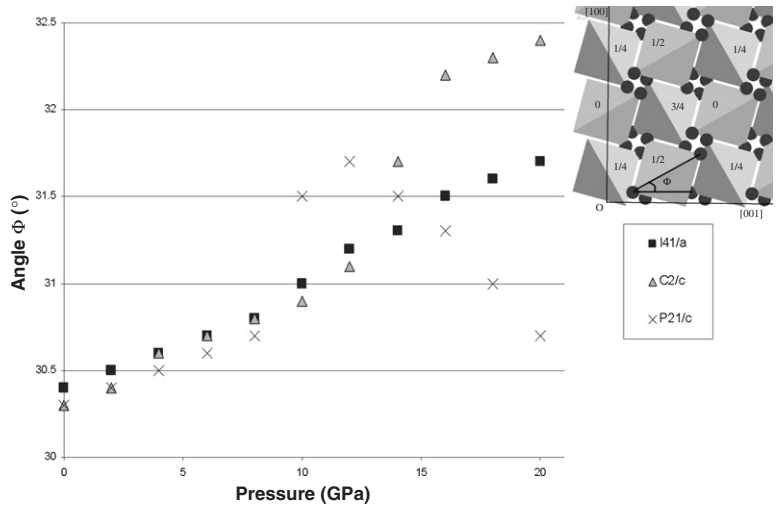

Figure 6. Angle Φ versus pressure. The scheme represents the projection of the tetrahedra in a unit cell of $LiYF_4$ on the (010) plane. The black atoms correspond to F anions.

the relaxed structures built from $I4_1/a$ does not change to lower symmetry. However, we can notice that the distortion observed for $S_P^{C2/c}$ and $S_P^{P2_1/c}$ affects the symmetry. Whereas at low

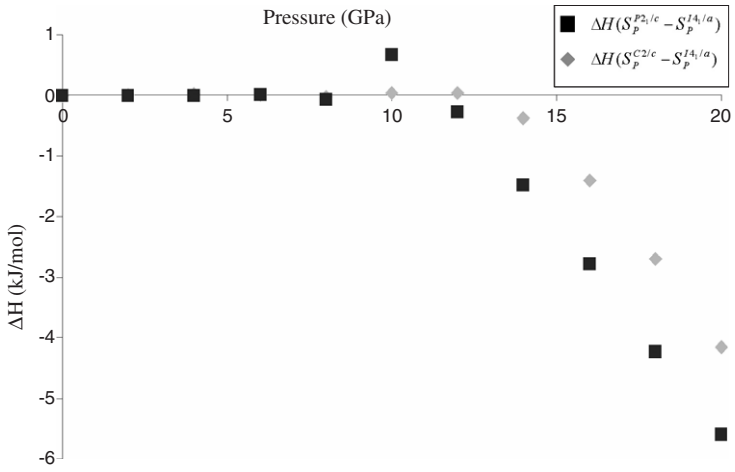

Figure 7. Enthalpy versus pressure. The enthalpies of $S_P^{I4_1/a}$ are taken as reference.

Table 1. Symmetry of the relaxed structures with a tolerance of 0.01 Å.

	Structures		
Pressure (GPa)	$S_P^{I4_1/a}$	$S_P^{C2/c}$	$S_P^{P2_1/c}$
0	$I41/a$	$I41/a$	$I41/a$
2	$I41/a$	$I41/a$	$I41/a$
4	$I41/a$	$I41/a$	$I41/a$
6	$I41/a$	$C2/c$	$C2/c$
8	$I41/a$	$C2/c$	$C2/c$
10	$I41/a$	$C2/c$	$P21/c$
12	$I41/a$	$C2/c$	$P21/c$
14	$I41/a$	$C2/c$	$P21/c$
16	$I41/a$	$C2/c$	$P21/c$
18	$I41/a$	$C2/c$	$P21/c$
20	$I41/a$	$C2/c$	$P21/c$

pressure the space group is $I4_1/a$, from 6 GPa the symmetry decreases to space group $C2/c$. Then for $S_P^{P2_1/c}$ we have a new symmetry from 10 GPa with the space group $P2_1/C$.

3.2. Enthalpies

Figure 7 shows enthalpies H, which in this case is the sum of electronic energies and the PV terms, for the systems $S_P^{C2/c}$ and $S_P^{P2_1/c}$ relative to $S_P^{I4_1/a}$. From 0 to 8 GPa the enthalpies of the relaxed structures are the same. Until this pressure, the volumes are the same so the internal energies are also identical. From 10 GPa the enthalpies of $S_P^{C2/c}$ and $S_P^{I4_1/a}$ remain identical but we observe a change for $S_P^{P2_1/c}$. We can notice that the internal energy of $S_{P=10}^{P2_1/c}$ is 4 kJ mol^{-1} higher than for $S_{P=10}^{I4_1/a}$ but it is compensated by the PV term since the volume of $S_{P=10}^{P2_1/c}$ is lower than the $S_{P=10}^{I4_1/a}$ volume. From 14 GPa, $S_P^{P2_1/c}$ structures are the most stable. $\Delta H(S_P^{P2_1/c} - S_P^{I4_1/a})$ and $\Delta H(S_P^{C2/c} - S_P^{I4_1/a})$ increase with the pressure but $\Delta H(S_P^{C2/c} - S_P^{P2_1/c})$ remains close to 1 kJ mol^{-1}.

Table 2. Elastic stiffness constants and mechanical moduli of scheelite $LiYF_4$ at 0 GPA. (Note: $G = 1/15(c_{11} + c_{22} + c_{33} - c_{12} - c_{13} - c_{23}) + 1/5(c_{44} + c_{55} + c_{66})$; $B = 1/9(c_{11} + c_{22} + c_{33}) + 2/9(c_{12} + c_{13} + c_{23})\nu = (3B - 2G)/[2(3B + G)]$; $E = (9 * B * G)/(3 * B + G)$.)

	Calc.	Exp. [24]
Elastic constants		
C_{11}	114 ± 2	121
C_{12}	53 ± 2	60.9
C_{13}	61 ± 1	52.6
C_{16}	-11 ± 2	−7.7
C_{33}	152 ± 2	156
C_{44}	37 ± 3	40.6
C_{66}	22 ± 3	17.7
Modulus		
B Bulk (GPa)	81	81
G Shear (GPa)	33	35
E Young (GPa)	87	92
ν Poisson	0.32	0.31

3.3. Mechanical properties

The bulk modulus (B) is important for the description of a crystal behaviour under pressure. From fitting with an equation of state, B was evaluated at 80 GPa [6, 8], 94.8 GPa [11] and 69 GPa [9] from experimental, DFT and empirical data respectively for the $I4_1/a$ space group. Fitting our P–V curves with the third order Birch Murnaghan equation of state we obtained a value of 76 GPa. Moreover, using Voigt's formalism for both numerical and experimental data the mechanical properties were calculated from the elastic constants at ambient pressure. From the results presented in table 2, we can see that the agreement between the moduli is very good. From the elastic constants we evaluated B at 81 GPa to be in very good agreement with the experimental value. The pressure dependence of the elastic constants for $S_P^{I4_1/a}$ is presented in figure 8. The elastic constants C_{11}, C_{12}, C_{13} and C_{33} show a strong pressure dependence, in contrast to C_{16} and C_{44} as experimentally measured on a range from 0 to 0.16 GPa [6]. Concerning C_{66} the value decreases as a function of the pressure to change of sign after 18 GPa. We can notice that a Born condition for the stability of crystals is that the eigenvalues of the elastic constants matrix be positive [25, 26]. Looking at these eigenvalues we can see that one of them becomes negative at 8 GPa. The eigenvector associated with the eigenvalue is $e_{xx} = -e_{yy} = -0.4763$, $e_{xy} = 0.7391$, $e_{zz} = e_{yz} = e_{xz} = 0$. A symmetry analysis of the strained cell following this vector gives a space group C_2/c.

3.4. Lattice dynamics

To study the mechanism of the pressure induced phase transition, we calculated the phonon dispersion curves of $S_P^{I4_1/a}$ within a range from 0 to 20 GPa, the pressure dependence of the Raman active modes is presented in figure 9. The vibrational modes above 250 cm^{-1} at 0 GPa are in agreement with experimental values by Sarantopoulou *et al* [4] within 10%. Three doublets were observed experimentally above 250 cm^{-1} from 7 GPa [4], namely ($E_g + B_g$) modes at 326 and 375 cm^{-1} and the ($A_g + B_g$) mode at 426 cm^{-1}. In our calculations at 0 GPa, they correspond to the ($E_g + B_g$) modes at 306/313 and 346/356 cm^{-1} and the ($A_g + B_g$) mode at 398/415 cm^{-1}. These doublets are separated even at 0 GPa and the relative difference between the first doublet ($E_g + B_g$) remains constant as function of the pressure. This behaviour deviates from experiment since a split of these two modes leads to a difference higher than

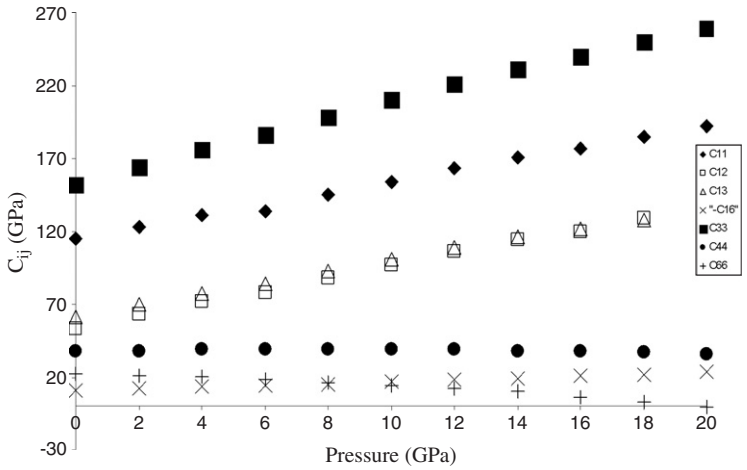

Figure 8. Elastic constants versus pressure of scheelite $LiYF_4$.

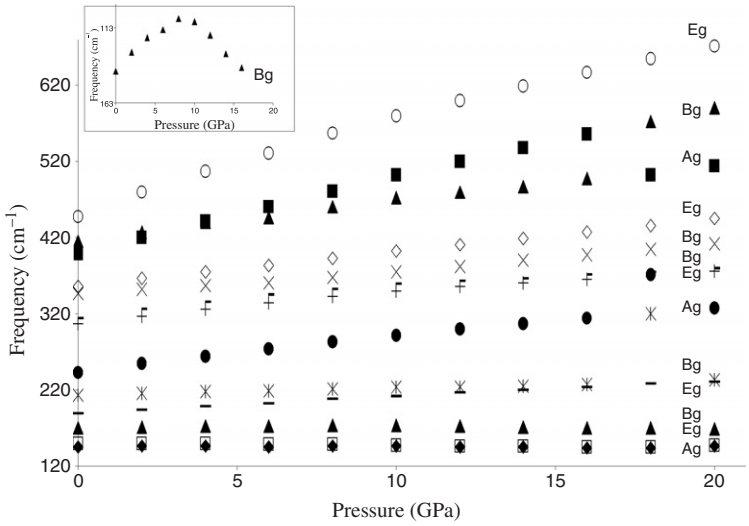

Figure 9. Pressure dependence of the Raman frequencies of scheelite $LiYF_4$.

40 cm^{-1} at 15 GPa. Concerning the second doublet ($E_g + B_g$), from 2 GPa upwards the relative difference increases and remains stable at around 30 cm^{-1} for higher pressure above 8 GPa. From Sarantopoulou *et al* [4] experiments, the split of this doublet is very low and does not exceed 20 cm^{-1} at 15 GPa, but the Wang *et al* [27] experimental results suggest that the splitting begins at 5 GPa and the difference between the two modes exceeds 20 cm^{-1} at 15 GPa. The splitting of the last doublet ($A_g + B_g$) takes place around 8 GPa in agreement with experiment [4]. But this different behaviour was not observed by Wang *et al* [27]. We calculated the $\partial\omega/\partial P$ slopes in the pressure intervals [0-8] and [10-16] GPa and the results are presented in table 3. The calculated slopes agree very well with experimental values at low pressure [4, 27]. In a general way the slopes at low pressure are more pronounced than at high pressure. However, we can notice three exceptions. Below 250 cm^{-1}, the frequency of the E_g mode decreases with increasing pressure. This behaviour was observed by Wang *et al* [27] for

Table 3. Pressure derivatives of frequencies of phonons of $LiYF_4$ at 0 K at low pressure (below 8 GPa) and high pressure (above 8 GPa).

	$d\omega/dP$ (cm^{-1} GPa^{-1})		
	[0-8]		[10-16]
Phonon modes	Exp.	Calc.	Calc.
A_g	—	0.23	−0.34
E_g	—	−0.29	−0.38
B_g	—	0.33	−0.50
E_g	—	2.33	1.97
B_g	1.13	1.07	0.53
A_g	5	5.07	3.75
E_g	6.6	4.47	2.67
B_g		4.86	2.00
B_g	4.54	2.33	3.92
E_g		4.57	4.30
B_g	5.77	5.53	4.12
A_g		10.37	8.93
E_g	14.43	13.53	9.69

pressure up to 17 GPa. For the first B_g mode on the range from 0 to 8 GPa the slope is positive but afterwards it becomes negative. Then for the fourth B_g mode the slope increases at high pressure.

The phonon dispersion curves for different pressures are presented in figure 10. At 4 GPa an energy gap appears at high frequency. From 8 GPa upwards, we can observe imaginary frequencies close to the Brillouin zone centre along the $[11\bar{1}]$ direction synonymous to dynamical instability. These frequencies correspond to translations of whole formula units along the *a* axis. These acoustical modes are linked to B_g and E_g optical modes as observed by Sarantopoulou *et al* [4]. All the frequencies observed for *k* along G–N are negative at 16 GPa. At the N point the LiF_4 tetrahedra tend to rotate around the *c* axis and the Li atoms start to translate along this axis. Moreover, for this same pressure additional imaginary frequencies appear close to the Brillouin zone centre along the [001] direction and another energy gap appears at high frequency. These frequencies correspond to translations of whole formula units along the *c* axis.

4. Discussion

From our results we defined four pointers to phase transition analysis: cell parameters, enthalpies, elastic properties and vibrational properties. Based on elastic and vibrational properties, the structure with the $I4_1/a$ space group is unstable above 8 GPa. Moreover from phonon dispersion curves another instability could take place at 16 GPa. At this pressure C_{66} is close to zero, that could be synonymous with a new mechanical instability [28].

The computed enthalpy points to a better stability of the $P2_1/c$ space group above 14 GPa for a temperature of 0 K, but it does not exclude that a phase transition exists between the $I4_1/a$ space group and C_2/c since the structures have the same enthalpy between 0 and 12 GPa. Moreover, above 14 GPa the difference in enthalpy is less than 1 kJ mol^{-1} between structures with $C2/c$ and $P2_1/c$ symmetries. From such a small energy difference it is difficult to conclude on the phase stability at this pressure. Indeed, even if the electronic energy is very well converged, at high pressure the error due to the Pulay stress induces an error around

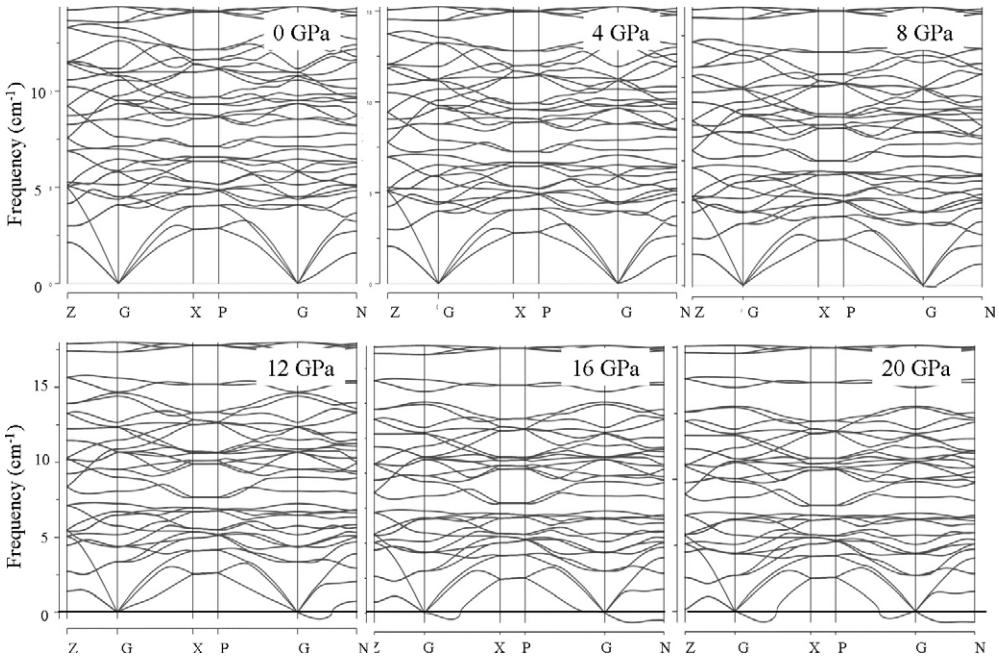

Figure 10. Phonon dispersion curves of scheelite $LiYF_4$ for 0, 4, 8, 12, 16 and 20 GPa. The path is defined in the direction of the quadratic Brillouin zone of the scheelite structure. The labels are adapted to the symmetry of the structure. $Z(1/2\ 1/2{-}1/2)$, G = $\Gamma(0\ 0\ 0)$, X(0 0 1/2), P(1/4 1/4 1/4), N(0 0.5 0).

1 kJ mol^{-1}. Moreover, the effect of the temperature can play a significant role as previously noticed by empirical dynamic molecular calculations [10]. In order to take into account the effect of temperature, the Gibbs free energy needs to be evaluated for all systems under investigation. Looking at the new symmetries adopted by the relaxed structures constructed from the $P2_1/c$ space group, it would seem that the transitions $I4_1/a \rightarrow C2/c \rightarrow P2_1/c$ are correct. Moreover, based on the volume analysis, these two transitions could be of the second order. Indeed, at 8 and 10 GPa the volumes of $I4_1/a$ and $C2/c$ structures are the same and at 16 GPa the volumes of $C2/c$ and $P2_1/c$ structures are also the same.

To understand the mechanism of transformation during the first transition we can look at the correlation between the bond lengths, ϕ angle evolution and the atomic motions associated with the soft modes. The softness of A_g, E_g and B_g Raman active modes appears around 8 GPa and is evident above 10 GPa. It could explain the anomalies observed around 7 GPa by Raman [4, 27] and luminescence [30] measurements. These three modes induce the rotation of the $LiYF_4$ not only in the ac plane but also around the c axis as well described by Salaün *et al* [3]. With increasing pressure, the Li–F distances decrease and ϕ increases. From 8 GPa the dynamical instability leads to a tilt movement explaining the formation of pentacoordinated lithium observed in $S^{P2_1/c}_{P>16}$ at high pressures.

Consequently, we conclude that the transition around 10 GPa is driven by a B_g soft optic mode coupled with a soft acoustic mode. This mechanism was previously observed for $BiVO_4$ and was associated with a proper ferroelastic phase transition [31]. This could confirm that $LiYF_4$ undergoes a pressure-induced ferroelastic phase transition as previously described [29]. To evaluate the order of the phase transition using the theoretical model from Grzechnik *et al* [29], further calculations at higher pressure are required.

5. Conclusion

DFT structure optimizations of $LiYF_4$ in the 0–20 GPa pressure range accurately point to one pressure induced phase transition, $I4_1/a \rightarrow C2/c$. Raman and luminescence anomalous measurements around 7 GPa can be explained by the softness of A_g, B_g and E_g low frequency modes. These three modes are associated with a tilting movement of the LiF_4 tetrahedra. We found a soft mode assisted transition similar to the temperature induced proper ferroelastic transition observed for $BiVO_4$. The second phase transition would be $C2/c \rightarrow P2_1/c$. But further calculations are required to evaluate the mechanisms of this phase transition and to confirm the existence of another structure at high pressure even if the wolframite structure seems to be excluded.

Acknowledgments

The authors wish to thank the Materials Design team for their help. We are grateful to CCI du Mans et de la Sarthe for providing calculation infrastructure.

References

[1] Choi B, Moon B, Seo H, Jeong J, Lee H and Seo W 2000 *Mater. Des.* **21** 567
[2] Ching W Y and Xu Y N 2001 *Phys. Rev.* B **63** 115101
[3] Salaün S, Bulou A, Rousseau M, Hennion B and Gesland J Y 1997 *J. Phys.: Condens. Matter* **9** 6957
Salaün S, Fornoni M T, Bulou A, Rousseau M, Simon P and and Gesland J Y 1997 *J. Phys.: Condens. Matter* **9** 6941
[4] Sarantopoulou E, Raptis Y S, Zouboulis E and Raptis C 1999 *Phys. Rev.* B **59** 4154
[5] Kroumova E, Aroyo M I, Perez Mato J M, Kirov A, Capillas C, Ivantchev S and Wondratschek H 2003 *Phase Transit.* **76** 155–70
[6] Blanchfield P, Saunders G A and Hailing T 1982 *J. Phys. C: Solid State Phys.* **15** 2081
[7] Errandonea D, Manjon F J, Somayazulu M and Häusermann D 2004 *J. Solid State Chem.* **177** 1087
[8] Grzechnik A, Syassen K, Loa I, Hanfland M and Gesland J Y 2002 *Phys. Rev.* B **65** 104102
[9] Sen A, Chaplot L S and Mittal R 2002 *J. Phys.: Condens. Matter* **14** 975
[10] Sen A, Chaplot L S and Mittal R 2003 *Phys. Rev.* B **68** 134105
[11] Li S, Ahuja R and Johansson B 2004 *J. Phys.: Condens. Matter* **16** S983
[12] Hohenberg P and Kohn W 1964 *Phys. Rev.* B **136** 864
[13] Kohn W and Sham L J 1965 *Phys. Rev* A **140** 1133
[14] Kresse G and Furthmüller J 1996 *Phys. Rev.* B **54** 11169
[15] Perdew J P, Burke K and Wang Y 1996 *Phys. Rev.* B **54** 16533
[16] Blöchl P E 1994 *Phys. Rev.* B **50** 17953
[17] Methfessel M and Paxton A 1989 *Phys. Rev.* B **40** 3616
[18] Monkhorst H J and Pack J D 1976 *Phys. Rev.* B **13** 5188
[19] Garcia E and Ryan R R 1993 *Acta Crystallogr.* C **49** 2053
[20] Francis G P and Payne M C 1990 *J. Phys.: Condens. Matter* **2** 4395
[21] Parlinski K, Li Z Q and Kawazoe Y 1997 *Phys. Rev. Lett.* **78** 4063
[22] Le Page Y and Saxe P 2002 *Phys. Rev.* B **65** 104104
[23] Zalkin A and Templeton D H 1964 *J. Chem. Phys.* **40** 501
[24] Blanchfield P, Saunders G A and Hailing T 1979 *J. Phys. C: Solid State Phys.* **12** 4673
[25] Vsin'ko G and Smirnov N A 2002 *J. Phys.: Condens. Matter* **14** 6989
[26] Born M and Huang K 1954 *Dynamical Theory of Crystal* (London: Oxford University Press) p 129
[27] Wang Q A, Bulou A and Gesland J Y 2002 *Preprint* cond-mat/0210491
[28] Karki B B, Ackland G J and ann Crain J 1997 *J. Phys.: Condens. Matter* **9** 8579
[29] Grzechnik A, Friese K, Dmitriev V, Weber H-P, Gesland J-Y and Crichton W A 2005 *J. Phys.: Condens. Matter* **17** 763
[30] Manjon J F, Jandl S, Syassen K and Gesland J Y 2001 *Phys. Rev.* B **64** 235108
[31] Benyuan G, Copic M and Cummins H Z 1981 *Phys. Rev.* B **24** 4098